Iranian Journal of Basic Medical Sciences

ijbms.mums.ac.ir

IJBMS

Development, characterization, and molecular dynamics simulation of resveratrol-loaded nanostructured lipid carriers for enhanced anti-oxidant and antityrosinase activity

Hoda Atapour-Mashhad [1,2#], Mohhamad Delkhosh [3#], Mojgan Nejabat [4], Shiva Golmohammadzadeh [1,2], Farzin Hadizadeh [4,5], Samaneh Rahamouz-Haghighi [6], Vahideh Mohammadzadeh [1], Zahra Tayarani-Najaran [7*]

[1] Nanotechnology Research Center, Pharmaceutical Technology Institute, Mashhad University of Medical Sciences, Mashhad, Iran
[2] Department of Pharmaceutics, School of Pharmacy, Mashhad University of Medical Sciences, Mashhad, Iran
[3] Medical Toxicology Research Center, Mashhad University of Medical Sciences, Mashhad, Iran
[4] Department of Medicinal Chemistry, School of Pharmacy, Mashhad University of Medical Sciences, Mashhad, Iran
[5] Biotechnology Research Center, Institute of Pharmaceutical Technology, Mashhad University of Medical Sciences, Mashhad, Iran
[6] Department of Pharmacodynamics and Toxicology, School of Pharmacy, Mashhad University of Medical Sciences, Mashhad, Iran
[7] Targeted Drug Delivery Research Center, Pharmaceutical Technology Institute, Mashhad University of Medical Sciences, Mashhad, Iran

ARTICLE INFO

Article type:
Original

Article history:
Received: Jul 17, 2026
Accepted: Aug 22, 2026

Keywords:
Anti-oxidant
Nanostructured lipid - carriers
Resveratrol
Reactive oxygen species - inhibition
Tyrosinase inhibitor

ABSTRACT

Objective(s): This study aimed to develop and characterize resveratrol-loaded nanostructured lipid carriers (Res-NLCs) to assess their preliminary potential as topical delivery systems, with a focus on antioxidant and antityrosinase properties.

Materials and Methods: Ten Res-NLC formulations (F1–F10) were prepared by high-shear homogenization combined with ultrasound. The formulations underwent comprehensive evaluation of morphology, particle size, long-term stability, and entrapment efficiency (EE%). Experimental findings were correlated with molecular dynamics (MD) simulations. In vitro performance was assessed by drug-release profiling (dialysis-bag diffusion), cytotoxicity and protective effects (MTT assay), reactive oxygen species (ROS) reduction (DCFH-DA), and anti-tyrosinase activity (L-DOPA assay).

Results: Formulation F10 exhibited excellent surface characteristics, including a z-average particle size of 144.0 nm, a narrow polydispersity index (PDI) of 0.117, a high negative zeta potential of -22.6 mV, favorable stability at lower temperatures, and optimal EE%. MD simulations confirmed superior molecular stability for F10 through compact cluster formation, consistent with its sustained long-term stability at 4 °C and 25 °C. In contrast, structural fragmentation observed in F2 accounted for its large particle size (>500 nm). The NLC systems exhibited a sustained-release profile, delivering 84% of the resveratrol over 48 hr. Furthermore, F10 significantly inhibited tyrosinase activity and effectively reduced intracellular ROS levels following hydrogen peroxide-induced stress.

Conclusion: The newly developed Res-NLC (F10) formulation serves as a promising, stable carrier for the sustained topical delivery of resveratrol, demonstrating notable antioxidant and antityrosinase performance, which warrants subsequent biological validation.

▶ Please cite this article as:
Atapour-Mashhad H, Delkhosh M, Nejabat M, Golmohammadzadeh Sh, Hadizadeh F, Rahamouz-Haghighi S, Mohammadzadeh V, Tayarani-Najaran Z. Development, characterization, and molecular dynamics simulation of resveratrol-loaded nanostructured lipid carriers for enhanced anti-oxidant and antityrosinase activity. Iran J Basic Med Sci 2026; 29: 1923-1937. doi: https://dx.doi.org/10.22038/ijbms.2026.97463.20959

Introduction

In recent years, the depletion of the ozone layer has led to significant issues with exposure to ultraviolet (UV) radiation (1). Solar UV radiation can cause various forms of skin damage, including DNA damage, cytokine release, keratinocyte hyperproliferation, and increased production of reactive oxygen species (ROS) (2). ROS contributes to skin aging through several mechanisms. As byproducts of cellular metabolism, ROS levels increase with age, leading to oxidative stress (3). Elevated ROS can damage crucial cellular components, including DNA, proteins, and lipids, thereby leading to cellular senescence (4). Additionally, ROS activates enzymes that degrade collagen and elastin in the extracellular matrix, causing loss of skin elasticity and the formation of wrinkles (3, 5). They also trigger inflammatory responses that further promote oxidative damage (5). Over time, the skin's capacity for self-repair decreases, leading to noticeable signs of aging, including fine lines and a rougher texture (4).

Additionally, UV rays are essential in the physiological

*Corresponding author: Zahra Tayarani-Najaran. Targeted Drug Delivery Research Center, Pharmaceutical Technology Institute, Mashhad University of Medical Sciences, Mashhad, Iran. Tel: +98-51-31801100, Fax: +98-51-38823251, Email: tayaraninz@mums.ac.ir
#These authors contributed equally to this work

© 2026. This work is openly licensed via CC BY 4.0.
This is an Open Access article distributed under the terms of the Creative Commons Attribution License (https://creativecommons.org/licenses), which permits unrestricted use, distribution, and reproduction in any medium, provided the original work is properly cited.

process of melanogenesis, which involves the production of melanin pigments in the skin (6). This process can occur directly by acting on melanocytes, the cells responsible for melanin production, or indirectly by releasing factors such as α-MSH (melanocyte-stimulating hormone-α) (7). The accumulation of melanin in the skin leads to hyperpigmentation, a condition characterized by darker or uneven skin tone (8). Melanin acts as a natural sunscreen, absorbing UV rays and providing essential protection for the skin. Therefore, skin pigmentation is considered a protective mechanism against harmful UV radiation (9). The enzyme tyrosinase, which functions as a polyphenol oxidase, is essential for melanin biosynthesis (10). Copper is a vital cofactor for tyrosinase activity (10). Tyrosinase catalyzes three key stages in the melanin production pathway: 1) Hydroxylation of the amino acid tyrosine to 3,4-dihydroxyphenylalanine (DOPA). 2) Oxidation of DOPA to dopaquinone. 3) Oxidation of 5,6-dihydroxyindole to indolequinone (10, 11). Inhibiting tyrosinase activity can reduce melanin production, thereby helping prevent or address pigmentation problems (12).

The use of skin care products has become a popular and effective method for protecting against the harmful effects of UV radiation. Many skin care formulations now incorporate active ingredients that help shield the skin from the damaging impacts of UV exposure (13).

In the present era, natural compounds have gained significant attention in the pharmaceutical and cosmetic sectors because of their diverse bioactivities, including UV absorption, anti-oxidant properties, and anti-inflammatory effects (14).

Resveratrol is a natural polyphenol present in plants like grapes, blueberries, rhubarb, and peanuts. It exhibits strong UV absorbance and potent anti-oxidant activity in both *in vitro* and in vivo settings (15). It can effectively boost the activity of nuclear factor-E2-related factor-2 (Nrf2), a crucial regulator of anti-oxidant defenses. This activation increases the levels of key anti-oxidant enzymes, including superoxide dismutase (SOD), catalase (CAT), and glutathione synthetase (GSH) (15, 16). This enhancement helps neutralize ROS and mitigate oxidative stress in cells (17).

The structural arrangement of resveratrol's hydroxyl groups enables it to effectively scavenge free radicals, thereby protecting the skin from oxidative damage associated with aging and various skin conditions (18). Additionally, resveratrol has been shown to reduce DNA damage caused by free radicals and to inhibit the production of ROS and nitric oxide (NO) (19, 20). Also, topical resveratrol use reduces protein carbonyl levels, an indicator of oxidative protein damage in treated skin (15). Despite its remarkable biological potential, free resveratrol is severely hindered by poor aqueous solubility, high chemical instability, and limited skin permeability. Encapsulating resveratrol within nanostructured lipid carriers (NLCs) effectively overcomes these limitations by protecting the active compound from degradation, enhancing skin penetration, and ensuring sustained release (15).

Resveratrol has gained considerable interest when formulated in NLCs and Solid Lipid Nanoparticles (SLNs) and has garnered significant attention due to its anti-oxidant properties and various potential applications (21). Studies have demonstrated that resveratrol-loaded NLCs exhibit enhanced properties compared to SLNs, particularly for dermal applications (21, 22). Notably, NLCs with smaller particle sizes and greater drug capacities have shown increased efficacy in delivering resveratrol (21). Research has also highlighted the superior skin-penetrating capabilities of NLCs, thereby facilitating efficient transport of resveratrol to the epidermis (19, 23). Although previous studies have investigated various resveratrol-loaded lipid nanoparticles, significant limitations in their long-term physical stability and burst-release behavior remain unaddressed. To bridge this critical research gap, the present study introduces a systematically optimized NLC formulation designed to substantially improve encapsulation efficiency and sustain drug release, thereby offering a more reliable delivery system for therapeutic applications.

Building on these considerations, the present study hypothesizes that the systematic optimization of lipid and surfactant compositions can significantly improve the structural stability, encapsulation efficiency, and skin-delivery performance of resveratrol-loaded nanostructured lipid carriers (Res-NLCs). To evaluate this hypothesis, a comprehensive formulation-development strategy was implemented across ten distinct Res-NLC configurations (F1–F10). The scientific rationale of this work integrates advanced physicochemical characterizations with molecular dynamics (MD) simulations to provide a deeper, atomistic-level understanding of the intermolecular interactions between resveratrol and the lipid matrix, thereby validating structural stability and encapsulation behavior. Ultimately, this study aims to establish a robust, stable, and efficient topical delivery system for enhanced anti-oxidant and anti-tyrosinase applications.

Materials and Methods

Materials

The following materials were used in this study: glyceryl behenate (Compritol® 888 ATO) and glyceryl palmitostearate (Precirol® ATO 5), which were generously provided by Gattefossé (Pvt. Ltd., France). Methanol and glyceryl tripalmitate (Tripalmtine) were obtained from Fluka (Germany). Additional materials included glycerol monostearate (GMS), cetyl palmitate, dimethyl sulfoxide (DMSO), Span® 80, phenylmethanesulfonyl fluoride (PMSF), N-acetylcysteine (NAC), L-3,4-dihydroxyphenylalanine (L-DOPA), 2' ,7'-dichlorofluorescein diacetate (DCFH-DA), 3-[4,5-dimethylthiazol-2-yl]-2,5 diphenyl tetrazolium bromide (MTT) and kojic acid were purchased from Sigma-Aldrich Co. (Deisenhofen Germany). Resveratrol (pharmaceutical grade) was procured from Tinab Shimi Khavarmianeh (Mashhad, Iran), while Tween 80 was sourced from Kimyagaran Emrooz (Tehran, Iran). Migliyol 812 (medium-chain triglycerides) was supplied by Oxin Chemistry Company (Razavi Khorasan, Iran). Analytical-grade methanol and ethyl acetate were obtained from Dr. Mojallali Industrial Chemical Complex (Tehran, Iran). HPLC-grade solvents, including methanol and acetonitrile, were obtained from Tedia (Fairfield, OH, USA), and tetrahydrofuran (THF) was purchased from Carlo Erba (Emmendingen, Germany). Dulbecco's Modified Eagle Medium (DMEM) and fetal calf serum (FBS) were sourced from Gibco (Grand Island, NY, USA), and doxorubicin (DOX; 10 mg/5 ml) was obtained from Ebewe (Unterach am Attersee, Austria).

Development of NLCs for resveratrol encapsulation

The Res-NLC formulations were prepared using a precise

combination of different solid lipids and surfactants to optimize encapsulation efficiency. The fabrication process comprised several sequential steps:

- Lipid phase preparation: A mixture consisting of surfactants, solid lipids, and liquid lipids was heated to slightly above their melting point. Resveratrol (0.25% w/w) was subsequently added to the molten lipid phase and stirred until fully dissolved.
- Aqueous phase heating: Simultaneously, the aqueous phase (deionized water) was heated to a temperature equivalent to that of the lipid phase.
- Homogenization: The aqueous and lipid phases were combined and homogenized in three consecutive stages using a high-shear homogenizer (Ultra-Turrax, Heidolph DIAX).
- The homogenization protocol was set as follows: 18000 rpm for 1.5 min, 23000 rpm for 1.5 min, and 28000 rpm for 1 min. Throughout this procedure, a water bath was used to maintain the temperature above the solid lipid's melting point.
- Sonication: The resulting pre-emulsion underwent ultrasonic processing using a probe sonicator (Bransonic, USA) at a 14% amplitude setting. The process involved seven 60-second cycles, with 15-second cooling intervals between cycles.
- Cooling and NLC formation: The final mixture was allowed to cool gradually to room temperature, facilitating the formation of stable NLCs (24).

For the comparative Res-emulsion formulation, the aqueous and lipid phases (with the same qualitative and quantitative composition as the Res-NLC) were combined and homogenized by gentle manual agitation at the same elevated temperature, without high-energy sonication.

Technical characterization

Physicochemical characterization

The physicochemical properties of the Res-NLCs, specifically particle size, polydispersity index (PDI), and zeta potential, were assessed using a Zetasizer Nano-ZS90 (Malvern, UK). Photon correlation spectroscopy (PCS) was employed at a 90° scattering angle and 25 °C. Samples were appropriately diluted with distilled water to ensure optimal detection conditions. Each analysis was performed in triplicate (25).

Transmission electron microscopy (TEM) analysis of Res-NLC

Morphological analysis was conducted via Transmission Electron Microscopy (TEM, LEO 912 AB, ZEISS, Germany) (26). The sample was diluted (1:50 v/v) with deionized water, homogenized in an ultrasonic bath for 1 min, and deposited onto carbon-coated copper grids. Negative staining was performed using a 2% (w/v) phosphotungstic acid solution, and the grid was subsequently dried in a desiccator at 25 °C. The prepared and stained Res-NLC sample was observed under a TEM instrument, specifically the LEO 912 AB from ZEISS, Germany.

Differential scanning calorimetry (DSC) analysis of Res-NLC

Thermal properties were investigated using Differential Scanning Calorimetry (DSC, METTLER TOLEDO DSC822e, Germany) (27). Approximately 3 mg of resveratrol, solid lipid, blank NLC, and loaded NLC samples were sealed in 40 µL aluminum pans. The heating range was 25–300 °C at a rate of 5 °C/min with a nitrogen flow rate of 50 ml/min. The DSC parameters, including melting point, onset, and enthalpy, were measured using STARe software.

Fourier transform infrared (FT-IR) analysis

Chemical structures and functional groups were examined via Fourier Transform Infrared (FT-IR) spectroscopy (Thermo Nicolet AVATAR 370) (28). Samples were prepared as KBr pellets and scanned over the 400–4000 cm^{-1} range.

Entrapment efficiency (EE%) of Res-NLC

2.3. EE% was determined using HPLC (Shimadzu) equipped with a Lichrospher C8 column (5 µm, 4.6 mm ID×25 cm, Hanbag, Dalian, China). The column temperature was maintained at 25 °C, and the injection volume was set to 20 µl. Chromatographic separation was achieved over a total run time of 25 min using a gradient mobile phase system (flow rate of 1 ml . min^{-1}) consisting of methanol and water (pH 2.2 with trifluoroacetic acid), varying from 10:90 to 90:10 (v/v) as detailed in Table S1. UV detection was performed at 275 nm (a representative standard chromatogram is shown in Figure S1).

To determine EE%, samples (2 ml) were initially filtered via centrifugal ultrafiltration units (Amicon Ultra, 30 kDa cutoff) at 13000 rpm and 4 °C for 10 min (Remi Elektrotechnik Ltd., Maharashtra, India). Both direct and indirect quantification methods were performed using a validated 13-point standard curve spanning a concentration range of 0.00012-0.5 mg/ml (analyzed in triplicate). In the direct method, 50 µl of the sample retained on the filter was dissolved in a 50:50 methanol-tetrahydrofuran mixture at 50 °C for 1 min, left at room temperature for 2 hr to allow lipids to sediment, and subsequently centrifuged at 13,000 rpm at 4 °C for 10 min prior to supernatant analysis. The EE% was calculated using the following equation:

$$EE\% = (C_E / C_T) \times 100$$

Where C_E is the entrapped drug, and C_T is the total amount of drug in the system. The calibration curve was plotted using Excel 2016, and the limit of detection (LOD) and limit of quantification (LOQ) values were determined using the LINEST function.

Stability assessment

Formulations were stored in siliconized glass vials at 4 °C, 25 °C, and 37 °C. Stability was monitored by tracking changes in color, homogeneity, particle size, PDI, and zeta potential at 1-, 3-, 6-, and 12-month intervals.

In vitro drug release study

The release profiles of selected Res-NLC and resveratrol-loaded emulsion (Res-emulsion) formulations were evaluated utilizing the dialysis membrane technique. For each formulation, a 1 ml sample was introduced into cellulose dialysis bags with a molecular weight cut-off of 12-14 kDa. These bags were subsequently immersed in 40 ml of phosphate-buffered saline (PBS, pH 7.4) and incubated at 37 °C in a shaking incubator at 100 rpm. Due to the lipophilic nature of resveratrol (Log P ≈ 3.1), which limits its aqueous solubility and creates a diffusion barrier, 5% (w/v) Tween 80 was incorporated into the phosphate buffer to maintain sink conditions and facilitate drug release into the aqueous medium.

To enhance drug solubility in the buffer, 5% (w/v) Tween 80 was incorporated into the phosphate buffer.

At predetermined time points (0.5, 1, 2, 4, 6, 8, 12, 24, and 48 hr), 2 ml aliquots were extracted from the release

Table 1. A: Composition of F10 formulation containing cetyl palmitate (CPT, N=44), medium chain triglyceride (MCT, N=20), and Tween 80 (TWN, N=51). B: Composition of F2 formulation containing tripalmitin (TRP, N=26), medium chain triglyceride (MCT, N=20), and Tween 80 (TWN, N=51).

A: Composition of F10 system	
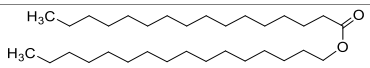	Cetyl palmitate (solid lipid), MW 480.86 72.78 mmol/l, 35 g/l, 43.81 N /1000 nm^3
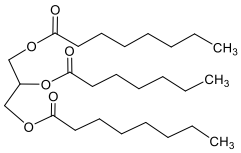	MCT (liquid lipid), MW 456.66 32.84 mmol/l, 15 g/l, 19.77 N/1000 nm^3
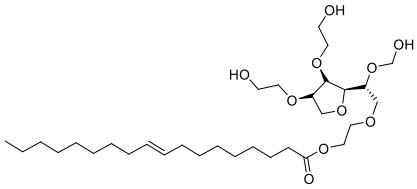	Tween 80, MW 590.80 84.63 mol, 50 g/l, 50.94 N/1000 nm^3
B: Composition of F2 system	
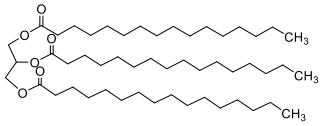	tripalmitin (solid lipid), MW 806.74 43.35 mmol/l, 35 g/l, 26.117 N/1000 nm^3
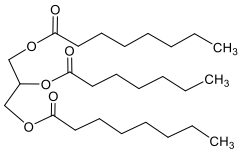	MCT (liquid lipid), MW 456.66 32.84 mmol/l, 15 g/l, 19.77 N/1000 nm^3
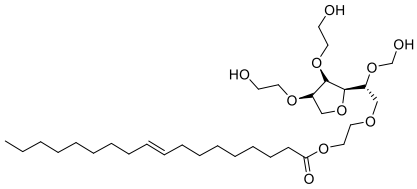	Tween 80, MW 590.80 84.63 mol, 50 g/l, 50.94 N/1000 nm^3

MCT: Medium-chain triglycerides

medium and immediately replaced with an equivalent volume of fresh buffer to maintain a constant total volume. The collected samples were analyzed by HPLC to determine the concentration of released resveratrol. The cumulative drug release (%) was assessed using the following equation (29):

$$M_n = C_n \times V_t + V_s \times \Sigma C_{(n-1)}$$

In this equation:
M_n represents the cumulative drug release (µg)
C_n denotes the drug concentration in the release medium at time t (µg/ml)
V_t is the total volume of the dissolution medium (ml)
V_s indicates the volume of sample that is withdrawn at each interval (ml)

Finally, the cumulative percentage of drug released was plotted as a function of time for both the Res-NLC and Res-emulsion systems to facilitate a comparative analysis.

Molecular dynamics system setup

The chemical structure of tripalmitin (TRP) and cetyl palmitate (CPT) and medium chain triglyceride (MCT) and Tween 80 (TWN) was drawn in ChemSketch (www.acdlab.com) and Perkin Elmer ChemDraw 16.0 (https://perkinelmer-chemdraw professional.software.informer.com/16.0/) converted into pdb and mol2 format in Perkin Elmer Chem3D 16.0 which were reused and energy minimized in MOE2019 (www.chemcomp.com) through Amber10EHT forcefield. The server Bio2Byte (www.bio2byte.be) was used to generate the corresponding itp and gro files using the Amber force field, which were then used as input files for GROMACS 2018 (30) running on an Ubuntu 16.04 system with a 32-core Ryzen CPU, 32 G of RAM, and an Nvidia GeForce 2080 GPU. The composition of these formulations is presented in Table 1.

F2 was selected as the representative formulation with the poorest physical performance because its initial particle size exceeded 500 nm (Table 2). This value was substantially above the predefined acceptable range of 100–300 nm for the nanostructured lipid carriers. Consequently, F2 was not included in the extended stability assessment presented in Table 3. In contrast, F10 was selected as the optimal formulation because it exhibited a particle size of 144.0 nm, a PDI of 0.117, a zeta potential of −22.6 mV, and consistent stability during storage at 4 °C and 25 °C for 12 months (Table 3). Therefore, F2 and F10 were selected for MD comparison as formulations representing the poorest and optimal experimental physicochemical performance, respectively.

For comparative MD assessment, energy minimization of the systems was performed for up to 50,000 steps using

Table 2. Ingredients of resveratrol-loaded nanostructured lipid Carriers (Res-NLCs, F1-F10) and corresponding particle size, polydispersity index, and zeta potential analysis at 24 hr and one month post-production

Formulation	Solid lipid (%)	MCT Oil (%)	Tween80 (%)	Span80 (%)	Resveratrol (%)	Z-Average size (nm)±SD	Polydispersity index (PDI)±SD	Zeta potential (mV)±SD
F1	Tripalmtin 3.5	1.5	4	1	0.25	490.5±3.6	0.112±0.013	-13.2±2.8
F2			5	-		537.1±5.1	0.145±0.009	-14.7±2.3
F3	Compritrol 3.5	1.5	4	1	0.25	437.8±4.3	0.345±0.024	-8.9±4.2
F4			5	-		274.2±6.2	0.293±0.021	-10.4±3.6
F5	Precirol 3.5	1.5	4	1	0.25	212.5±3.8	0.178±0.016	-13.4 ± 3.5
F6			5	-		178.8±1.9	0.202±0.030	-6.82±3.4
F7	GMS 3.5	1.5	4	1	0.25	231.6±4.5	0.298±0.022	-13.6±3.1
F8			5	-		306.7±2.9	0.332±0.018	-19.0 ± 2.86
F9	Cetyl palmitate 3.5	1.5	4	1	0.25	77.5±3.5	0.223±0.025	-23.7±4.1
F10			5	-		144.0±5.1	0.117±0.013	-22.6±3.5

MCT: Medium-chain triglycerides

the steepest-descent method. For bonded interactions, the LINCS algorithm was used. Nonbonded electrostatic and van der Waals interactions were calculated using the Particle Mesh Ewald (PME) method (cutoff radius of 1.2 nm for long-range electrostatic) and Verlet scheme (cutoff distance of 1.2 nm for short-range van der Waals), respectively (31). Both F2 and F10 systems were equilibrated at 310°K for 100 ps using a V-rescale thermostat for NVT at 1 bar pressure for 100 ps (*via* Berendsen barostat for NPT) (32, 33). Both systems were subjected to an MD simulation run with a time step of 2 fs for 250,000,000 steps, corresponding to 500 ns. Coordinates were saved every 5000 steps. A total of 50,000 steps were recorded (32).

For the F10 system, a box measuring 10×10×10 nm was constructed. According to the experiment, the cetyl palmitate (CPT) concentration was 35 g/l, equal to 3.5%. Hence, the number (N) of CPT in 1000 nm3 considering its MW of 480.86 and Avogadro's number of 6.02 x 10^{23}, N=43.81 (or 44). Accordingly, the MCT concentration was 15 g/l, equal to 1.5%, and N was 19.77 (or 20), and the TWN concentration was 50 g/l, equal to 5%, and its N was 50.94 (or 51). We placed these N of CPT, MCT, and TWN in the simulation box by means of the insert-molecules command in GROMACS (Table 1A).

For the F2 system, we built a box with dimensions of 10×10×10 nm. According to the experiment, the TRP concentration was 35 g/l, equal to 3.5%. Hence, the number (N) of TRP in 1000 nm^3 considering its MW of 806.74 and Avogadro's number of 6.02 x 10^{23}, N=26.11 (or 26). Accordingly, the MCT concentration was 15 g/l, equal to 1.5%, and N was 19.77(or 20), and Tween 80 (TWN) concentration was 50 g/l, equal to 5%, and its N was 50.94 (or 51). We placed these N of CPT, MCT, and TWN in the simulation box by means of the insert-molecules command

Table 3. Stability evaluation of the selected resveratrol-loaded nanostructured lipid carrier (Res-NLC, formulation F10) at different temperatures (4 °C, 25 °C, and 37 °C) over 1, 3, 6, and 12 months

Code	Temperature (°C)	Time (months)	Z-Average size (nm)±SD	Polydispersity index (PDI)±SD	Zeta potential (mV)±SD	Homogeneity/Color
F10	4	0	144.0±5.1	0.117±0.013	-22.6±3.5	Homogenous/White
		1	143.1±2.1	0.100±0.035	-19.3±3.2	
		3	144.8±2.5	0.102±0.028	-17.3±1.8	
		6	138.1±1.6	0.112±0.020	-15.2±1.2	
		12	191.3±4.2	0.108±0.034	-17.4±2.5	
	25	1	142.4±3.5	0.080±0.021	-17.7±2.5	
		3	143.7±2.6	0.069±0.018	-14.0±2.6	
		6	153.0±2.9	0.112±0.024	-16.3±3.4	
		12	183.8±3.8	0.114±0.042	-12.0±2.4	
	37	1	150.7±2.9	0.101±0.029	-17.8±1.4	
		3	369.1±3.4	0.095±0.026	-14.8±2.1	
		6	383.4±3.6	0.083±0.018	-12.8±2.5	
		12	385.4±4.1	0.267±0.027	-9.79±3.1	

NLC: Nanostructured lipid carriers

in GROMACS (Table 1B).

Both boxes were solvated; the density of water is 33 per nm3, and for a box of 1000 nm^3, the number of water molecules was estimated to be 33000.

In vitro cellular bioassays and functional analysis

Cell viability assessment analysis (MTT assay)

The impact of Res-NLC formulations and hydrogen peroxide (H_2O_2) on the viability of B16F10 melanoma cells was evaluated using the MTT reduction assay (34). Initially, B16F10 cells were seeded in a 96-well plate at a density of 10,000 cells per well and allowed to adhere overnight. The following day, cells were exposed to a series of Res-NLC (F10) ranging from 1.5 to 12.5 µg/ml and incubated for an additional 24 hr. Furthermore, DOX (5 µg/ml) was used as a positive control. Following the treatment period, 100 µl of MTT solution (5 mg/ml) was added to each well, and the plate was incubated for an additional 4 hr. After carefully removing the culture medium, 100 µl of DMSO was added to each well to dissolve the resulting formazan crystals. Finally, the absorbance of each sample was recorded at 570 nm using a BioTek Synergy H4 microplate reader (USA) (35).

Determination of intracellular reactive oxygen species (ROS) levels

The quantification of intracellular ROS was performed utilizing the fluorometric probe 2', 7'-dichlorofluorescein diacetate (DCFH-DA). B16F10 melanoma cells were seeded into 96-well plates (10000 cells per well) and subsequently treated with varying concentrations (0-12.5 µg/ml) of either free resveratrol, blank (drug-free) NLCs, or Res-NLC formulation. N-acetylcysteine (NAC, 5 µM) was used as a positive control (36). Untreated cells served as the negative control. Each experimental condition was conducted in triplicate over a 24-hour incubation period. Following the treatment, cells were incubated with 10 µM DCFH-DA. To stimulate ROS generation, the cells were exposed to 7.5 mM hydrogen peroxide at 37 °C for 2 hr. During this process, DCFH is oxidized by H_2O_2 to form the highly fluorescent compound dichlorofluorescein (DCF), thereby enabling quantification of ROS levels. The resulting DCF fluorescence intensity was measured using a VICTOR X5 microplate reader (PerkinElmer, USA) with excitation at 485 nm and emission at 530 nm. The ROS levels were normalized and expressed as a percentage of the H_2O_2-treated control group (set to 100%). This technique offers a robust and dependable approach for assessing intracellular oxidative stress through fluorescence quantification (36).

Cellular tyrosinase activity assay

To assess tyrosinase activity, B16F10 melanoma cells were seeded at a density of 100,000 cells per well in 12-well plates and incubated overnight. The following day, cells were treated for 24 hr with the following experimental groups: free resveratrol (1.5 µg/ml), Res-NLC (F10) (1.5 µg/ml), and blank NLC (at an equivalent lipid concentration). Kojic acid (2 mM) was employed as the positive control. Untreated cells were used as the negative control, and their activity was established as the baseline (100%) for normalization. Subsequently, cells were harvested and transferred into microcentrifuge tubes. The cell suspensions were centrifuged at 1000 rpm for 5 min, and the resulting pellets were washed with phosphate-buffered saline (PBS). Cell lysis was initiated by adding 100 µL of lysis buffer containing 1% Triton X-100, 100 mM sodium phosphate buffer (pH 6.8), and 0.1 mM phenylmethylsulfonyl fluoride (PMSF). Lysis was achieved through a freeze-thaw cycle, with PMSF supplementation every 30 min to preserve enzymatic stability. Following lysis, the samples were centrifuged at 10000 rpm for 20 min at 4 °C to isolate the supernatant from cellular debris. To account for variations in cell numbers, the total protein concentration in each lysate was quantified using a standard BCA (Bicinchoninic Acid) protein assay kit (normalization procedure). For the tyrosinase assay, a 100 µl aliquot of the supernatant was combined with 100 µl of L-DOPA (5 mM) in a 96-well microplate and incubated at 37 °C for 2 hr in the dark. Tyrosinase activity was subsequently quantified by measuring the absorbance of the solution at 475 nm (37) and calculated as a percentage relative to the negative control.

Data analysis

Statistical analysis was performed using one-way ANOVA via GraphPad Prism 9.0 (GraphPad Software, Inc., USA), followed by Tukey's *post-hoc* test. Before ANOVA, the normality of the data distribution was assessed using the Shapiro-Wilk test, and homogeneity of variances was evaluated using Levene's test. Differences were considered statistically significant at a threshold of $P<0.05$.

Results

Particle size, polydispersity index, and zeta potential analyses of the Res-NLC

The ingredients, particle-size analysis, polydispersity index (PDI), and zeta potential of the Res-NLCs are summarized in Table 2 and Figure 1. The newly prepared formulations (F1-F10) exhibited particle sizes ranging from approximately 77 nm (F9) to 537 nm (F2). The PDI values ranged from about 0.11 to 0.35, indicating a uniform particle size distribution. Additionally, the zeta potential measurements for the Res-NLC formulations ranged from -6 mV to -23 mV, indicating their suspension stability.

Long-term stability

The evaluation of the surface properties and physicochemical characteristics established strict quantitative acceptance criteria for selecting the optimal formulation: (1) a targeted z-average particle size within the optimal topical absorption range of 100–300 nm, (2) a narrow polydispersity index (PDI<0.3) indicating a homogenous size distribution, (3) an absolute zeta potential > 20 mV ensuring sufficient colloidal stability (38). Based on these quantitative thresholds, formulations F4, F5, F6, F7, and F10 successfully met the size and physical criteria. Although formulation F9 exhibited the smallest size (77.5 nm), it fell below the ideal lower threshold of 100 nm, posing a significant risk of physical instability and excessive systemic permeation (38). Among the qualified candidates, formulation F10 was ultimately selected as the optimal choice because its entrapment efficiency was confirmed, and it exhibited an optimal particle size of 144.0 nm, a low PDI of 0.117, and a high zeta potential of -22.6 mV.

After one month of storage at temperatures of 4 °C, 25 °C, and 37 °C, we assessed particle size, polydispersity index (PDI), and surface charge, with results summarized in Table S2 (in the supplementary file). Based on the results, only F10 demonstrated consistent stability across all storage conditions, exhibiting minimal changes in the measured

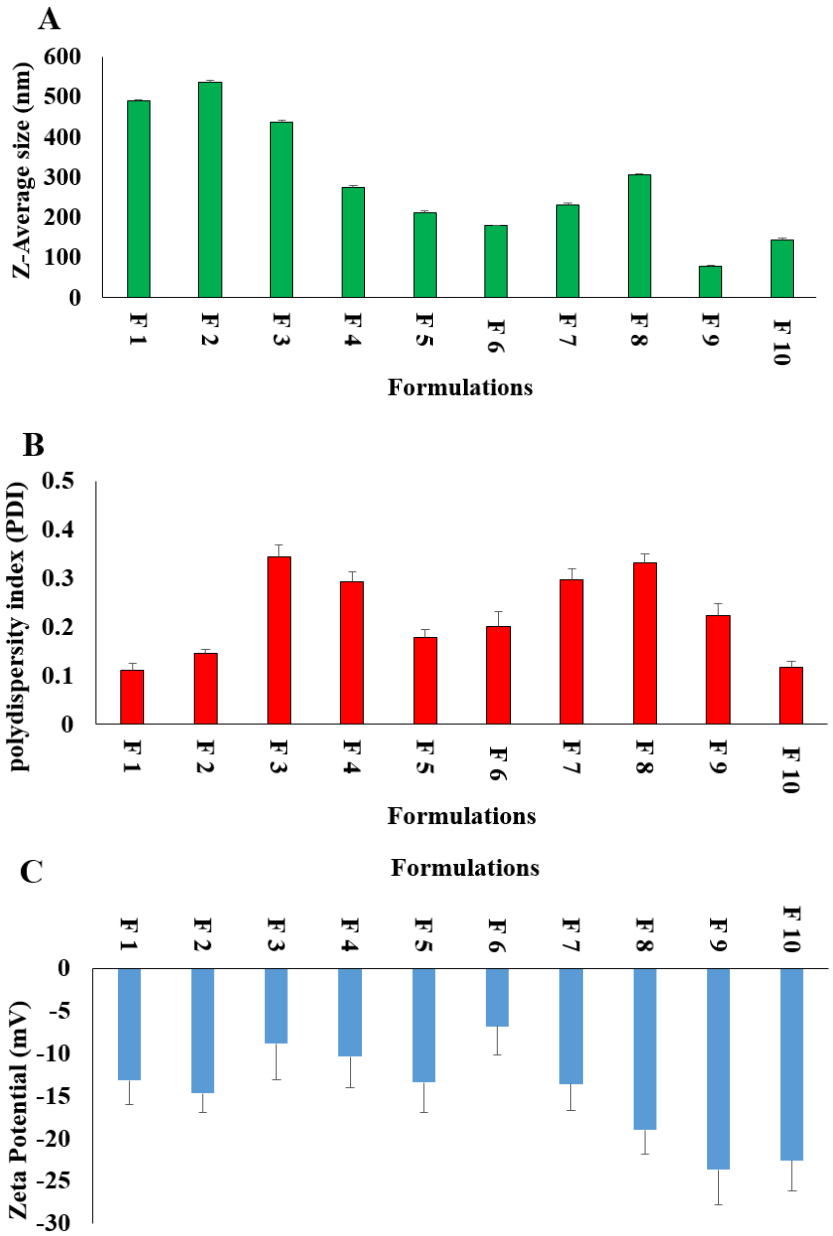

Figure 1. Illustration of the physicochemical properties of resveratrol-loaded nanostructured lipid carriers (Res-NLCs, F1-F10(: (A) Z-average particle size (in nm), (B) Polydispersity index (PDI), and (C) Zeta potential (in mV)

parameters at 4 °C, 25 °C, and 37 °C. In contrast, F4, F5, and F6 showed significant increases in particle size when stored at 37 °C, indicating that elevated temperatures adversely affect stability. Additionally, formulation F7 exhibited sedimentation across all three temperature conditions.

Conversely, formulation F10 (utilizing cetyl palmitate and Tween 80) successfully maintained its dimensions within the optimal 100-300 nm range (144.0 nm), along with a low PDI and stable physicochemical properties, making it the ideal candidate for further long-term stability assessments, including measuring particle size, PDI, and zeta potential at 3, 6, and 12 months (Table 3), and physicochemical characterization like TEM, differential scanning calorimetry (DSC), Fourier-transform infrared (FT-IR) spectroscopy, and evaluation of entrapment efficiency (EE).

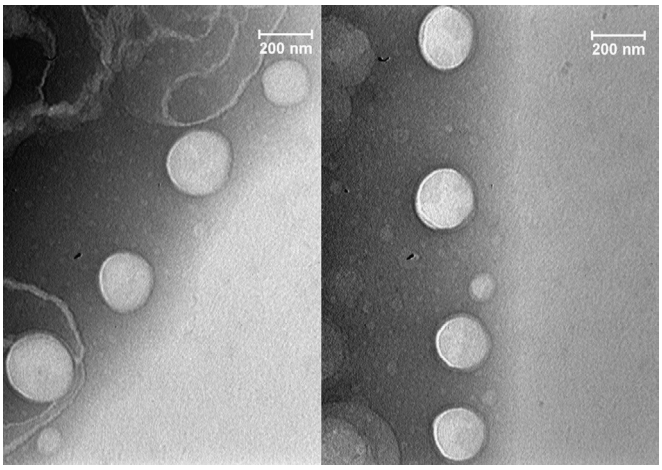

Figure 2. Transmission electron microscopy (TEM) image of the selected resveratrol-loaded nanostructured lipid carrier (Res-NLC, formulation F10)

TEM analysis

The microscopic morphology of F10 is illustrated in

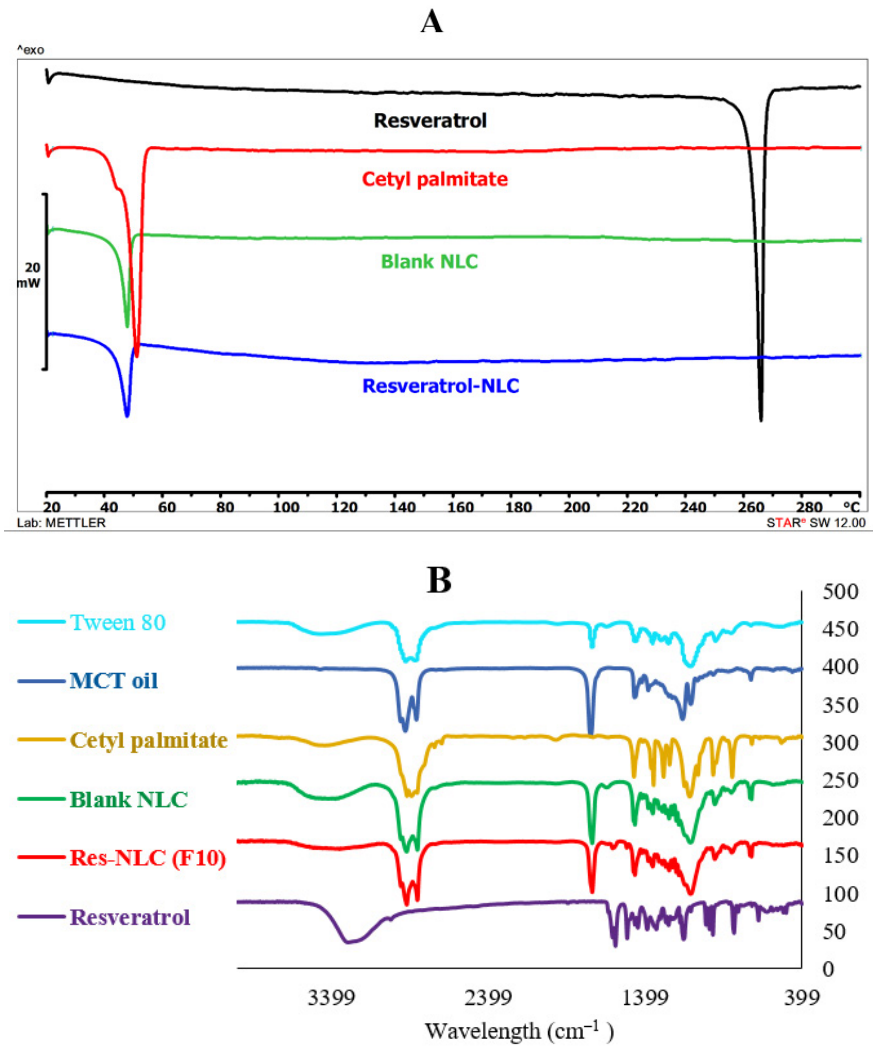

Figure 3. (A) Differential scanning calorimetry (DSC) thermograms and (B) Fourier transform infrared (FT-IR) spectra of resveratrol, solid lipid (cetyl palmitate), MCT oil, blank nanostructured lipid carrier (Blank NLC), and F10 (resveratrol-loaded NLC, Res-NLC), recorded within the 400-4000 cm^{-1} spectral range

Figure 2. The TEM measurement of F10 demonstrated that the nanoparticles are spherical, with an average particle size of approximately 200 nm.

Thermal analysis of the prepared Res-NLC

Differential Scanning Calorimetry (DSC) was employed to characterize the thermal behavior of the prepared formulations. The initial analysis of pure resveratrol and the solid lipid (cetyl palmitate) confirmed their characteristic melting points, with endothermic peaks observed at 263 °C and 50 °C, respectively. As illustrated in the DSC thermogram in Figure 3A, the characteristic melting peak of resveratrol was completely suppressed following its encapsulation within the NLC matrix, suggesting the drug exists in an amorphous state. Furthermore, a depression in melting point was observed for both the blank and drug-loaded NLCs compared with the bulk lipid. This shift was corroborated by enthalpy measurements, where the bulk cetyl palmitate exhibited a significantly higher enthalpy (240.20 J/g) compared to that of the lyophilized drug-free NLC (76.84 J/g); this reduction in enthalpy is primarily attributed to the decreased crystallinity and the formation of a less ordered, more amorphous structure within the NLC matrix during the production process.

Fourier transform infrared (FT-IR) analysis

The FT-IR analysis (Figure 3B) was used to evaluate the structural integrity and compatibility of the components in the Res-NLC formulation (F10) over the 400–4000 cm^{-1} range. The spectrum of pure resveratrol exhibited a characteristic broad absorption band between 3200 and 3500 cm^{-1}, attributed to the stretching vibrations of hydroxyl (–OH) groups. Furthermore, the aromatic skeleton was confirmed by prominent peaks at 1605, 1511, and 1442 cm^{-1} corresponding to C=C stretching vibrations. The bands observed at 1585, 1146, and 965 cm^{-1} were assigned to C–O stretching and olefinic C=C bending, while the peak at 1449 cm^{-1} was indicative of $–CH_2$ bending vibrations.

The individual spectra of the excipients, including cetyl palmitate, Tween 80, and MCT oil, displayed functional groups characteristic of their lipid and surfactant nature. Cetyl palmitate showed C-H stretching vibrations (2850-2920 cm^{-1}), and a carbonyl (C=O) stretch near 1730 cm^{-1}. Tween 80 demonstrated a broad -OH stretching band (approx. 3470 cm^{-1}), C-H stretching (2853 and 2920 cm^{-1}), a C=O stretch (approx. 1734 cm^{-1}), and a C-O-C stretch band

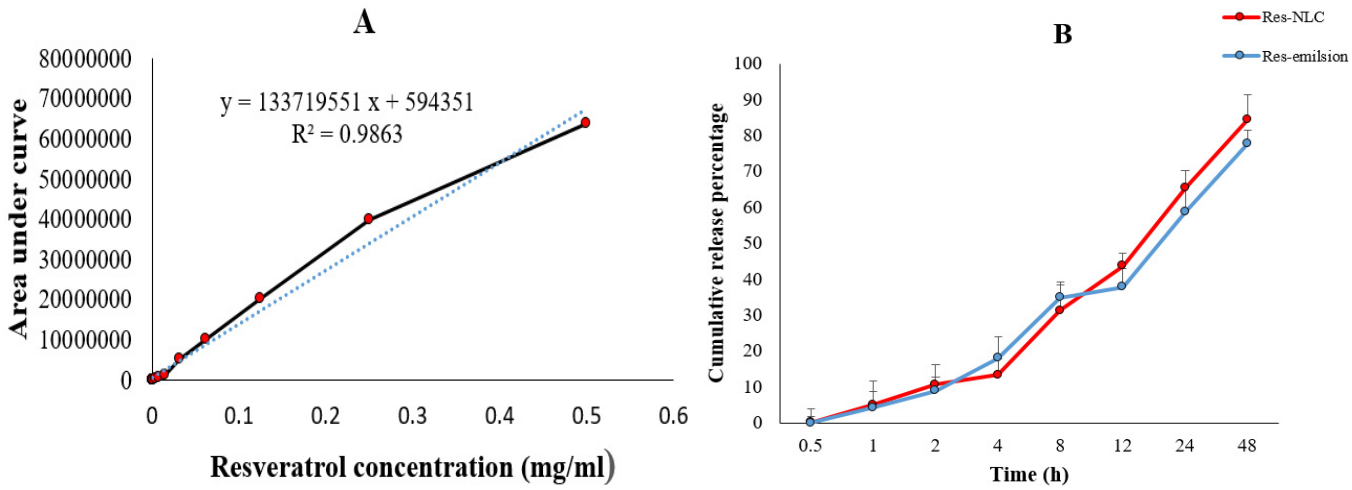

Figure 4. (A) Resveratrol standard calibration curve for concentration range (0.00012-0.5 mg/ml). (B) Cumulative release of F10 (resveratrol in resveratrol-loaded nanostructured lipid carrier, Res-NLC) and Res-emulsion over 48 hr
Data represent the mean±standard deviation (SD) based on three independent biological replicates (n=3).

at 1095 cm^{-1}. The MCT oil spectrum was consistent with triglyceride structures, showing characteristic C-H (2850-2920 cm^{-1}) and C=O (approx. 1740 cm^{-1}) stretching bands.

Importantly, the Res-NLC formulation exhibited no novel peaks or significant spectral shifts, suggesting that the constituent components remained chemically stable and did not undergo deleterious interactions during encapsulation.

Entrapment efficiency (EE%)

The EE% was determined using high-performance liquid chromatography (HPLC). The HPLC chromatogram of resveratrol is shown in Figure S1 of the supplementary file. Resveratrol demonstrated a retention time of approximately 13-14 min. The calibration curve for resveratrol concentrations (Figure 4A) showed a linear response with a squared correlation coefficient (R2) of 0.9863, confirming acceptable linearity for the intended quantitative analysis within the tested range. LOD and LOQ were determined to be 0.05 mg/ml and 0.15 mg/ml, respectively (based on the response standard deviation and the slope).

The entrapment efficiency (EE%) of the Res-NLC system F10 was assessed using the indirect method at 0 and 6 months, yielding values of 97.92±2.10% and 96.56±1.86%, respectively. These results indicate that the EE% for the desired formulation remains high over the evaluation period.

The drug release profile of Res-NLC and Res-emulsion

The *in vitro* release characteristics of resveratrol from two distinct delivery systems, Res-NLC (F10) and a conventional Res-emulsion, were evaluated over 48 hr, as illustrated in Figure 4B. Both formulations demonstrated a sustained and gradual release profile. Notably, the Res-NLC formulation exhibited a higher cumulative release, delivering 84% of the encapsulated drug within 48 hr, compared to 77% for the Res-emulsion. This difference in release behavior is primarily attributed to variations in particle size and structural organization resulting from different preparation methods (high-shear homogenization/sonication vs. manual stirring), while the compositional factors remained consistent.

Molecular dynamics studies

The MD simulations of the F2 and F10 systems provide valuable insights into their structural stability and clustering behavior. Both systems were simulated for 500 ns, with results indicating significant differences in their clustering dynamics and stability (Figures 5A & 5B). As shown, system F10 formed one small cluster and one major cluster on the side of the simulation box (10 x 10 x 10 nm). In contrast, system F2 formed two medium and two small clusters at the sides of the simulation box. The radius of gyration (R_g) for both F2 and F10 was almost constant, 45.84±0.04 Å for F2 and 45.94±0.04 Å for F10 (Figure 5C). Also, the Root Mean Square Deviation (RMSD) for the systems reached a plateau after 100 ns, with values of 59.62±0.044 Å for F2 and 61.06±4.85 Å for F10 (Figure 5D). Both systems reached an apparent RMSD plateau after approximately 100 ns, while their nearly constant, comparable Rg values indicated that their overall dimensions remained stable throughout the simulation. However, because the R_g and RMSD values overlapped substantially, these parameters do not provide strong evidence of a major difference in global structural stability between F2 and F10. To quantitatively bridge the molecular simulation data with the experimental physical observations, the clustering organization of systems F10 and F2 was evaluated. The clustering analysis showed a more coherent and dominant cluster in F10, whereas F2 exhibited a more fragmented distribution. This difference in organization may be consistent with the smaller particle size of F10 (144 nm) and its better experimental stability at 4 °C and 25 °C. Nevertheless, given the comparable R_g values and overlapping RMSD profiles, these observations should be interpreted as differences in clustering organization rather than definitive evidence that F10 possesses superior global molecular stability. The fragmented clustering observed for F2 may be associated with its larger initial particle size (>500 nm), although this relationship requires confirmation through additional quantitative analyses.

Cell viability

To evaluate the *in vitro* cytotoxicity, B16F10 cells were treated with the Res-NLC (F10) formulation at concentrations ranging from 1.5 to 12.5 µg/ml for 24 hr. The MTT assay indicated that neither the blank NLC, free resveratrol, nor the Res-NLC formulations exhibited

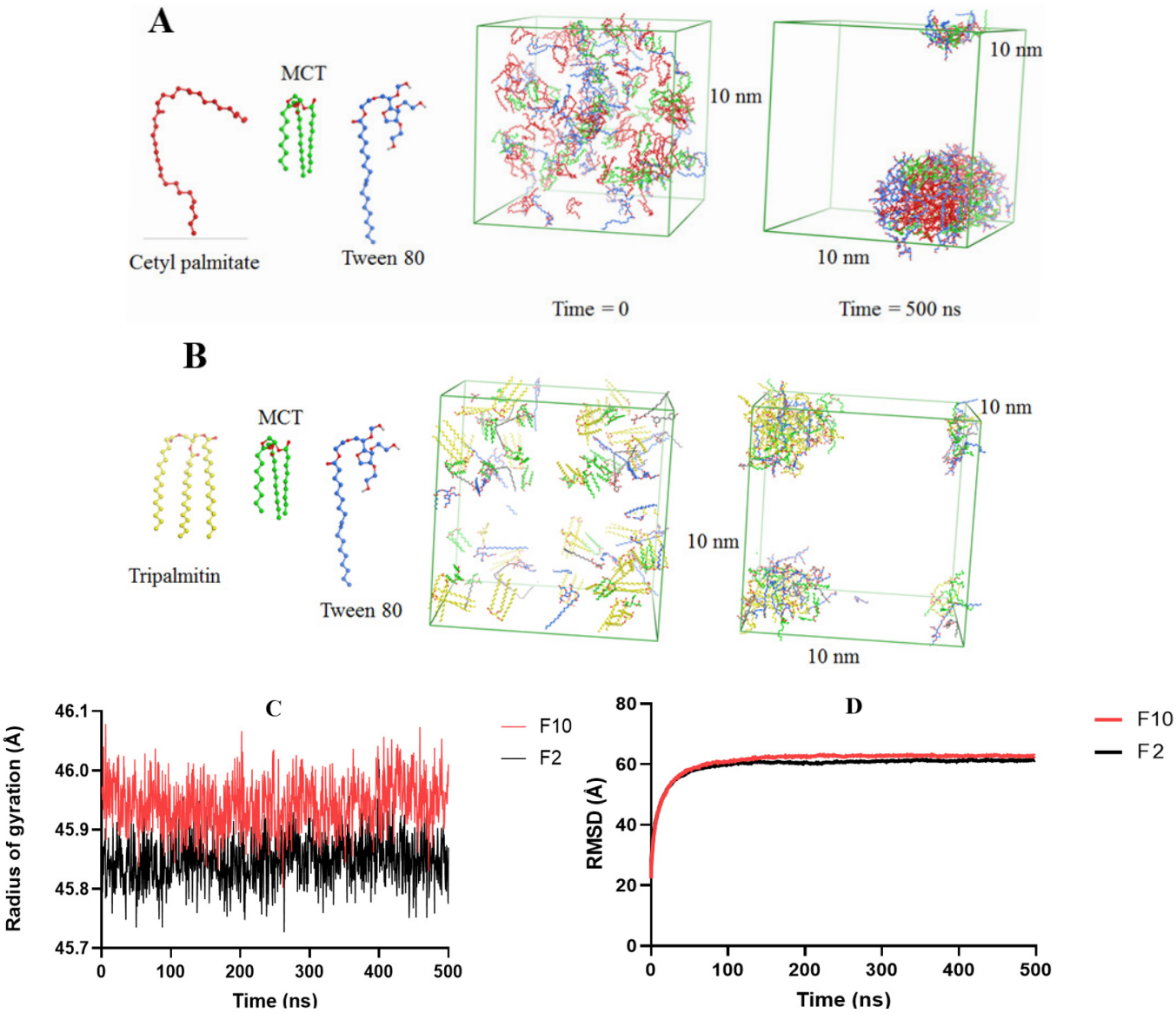

Figure 5. (A) A built 10 x 10 x 10 nm system composed of cetyl palmitate (CPT, N=44), medium-chain triglyceride (MCT, N=20), and Tween 80 (TWN, N = 51) for the F10 formula at time zero and after 500 simulations. (B) A built 10 x 10 x 10 nm system composed of tripalmitin (TRP, N=26), medium-chain triglyceride (MCT, N=20), and Tween 80 (TWN, N=51) for the F2 formula at time zero and after 500 ns of simulation. (C) Radius of gyration (Rg) for systems F10 (red) and F2 (black). The mean values were 45.94±0.04 Å for F10 and 45.84±0.04 Å for F2. (D) Root mean square deviation (RMSD) for systems F10 (red) and F2 (black). The mean values were 61.06±4.85 Å for F10 and 59.62±0.044 Å for F2

significant cytotoxicity compared to the untreated control group (data not depicted). Furthermore, the cytotoxic effect of hydrogen peroxide (H_2O_2) on cell viability was determined using the same assay. Exposure to 7.5 mM H_2O_2 resulted in a substantial decrease in cell viability (approximately 70%); consequently, this concentration was selected for subsequent ROS induction experiments.

Modulation of intracellular ROS levels

The potential of the formulated carriers to modulate ROS in B16F10 melanoma cells was assessed by quantifying the absorbance of Dichlorodihydrofluorescein (DCF) following H_2O_2 challenge. Experimental data demonstrated that H_2O_2 exposure markedly elevated intracellular ROS levels. Conversely, pretreatment with Res-NLC (F10) exhibited a robust inhibitory effect on ROS generation, providing significant protection against H_2O_2-induced cytotoxicity in a concentration-dependent manner (Figure 6A). In comparison, free resveratrol provided less effective protection than the Res-NLC (F10) formulation. Furthermore, the blank NLC formulation was observed to exert a similar reduction in oxidative stress to that of the drug-loaded NLCs.

Antityrosinase activity assessment

As depicted in Figure 6B, the anti-tyrosinase potential of the prepared formulations was evaluated in B16F10 cells. The results demonstrated that free resveratrol, Res-NLC, and blank NLCs, all administered at 1.5 µg/ml, significantly inhibited tyrosinase activity. Importantly, the resveratrol-loaded NLCs displayed superior efficacy in suppressing the enzyme compared to free resveratrol. Kojic acid was employed as a positive control, confirming the expected antityrosinase response. Each sample analyzed contained a

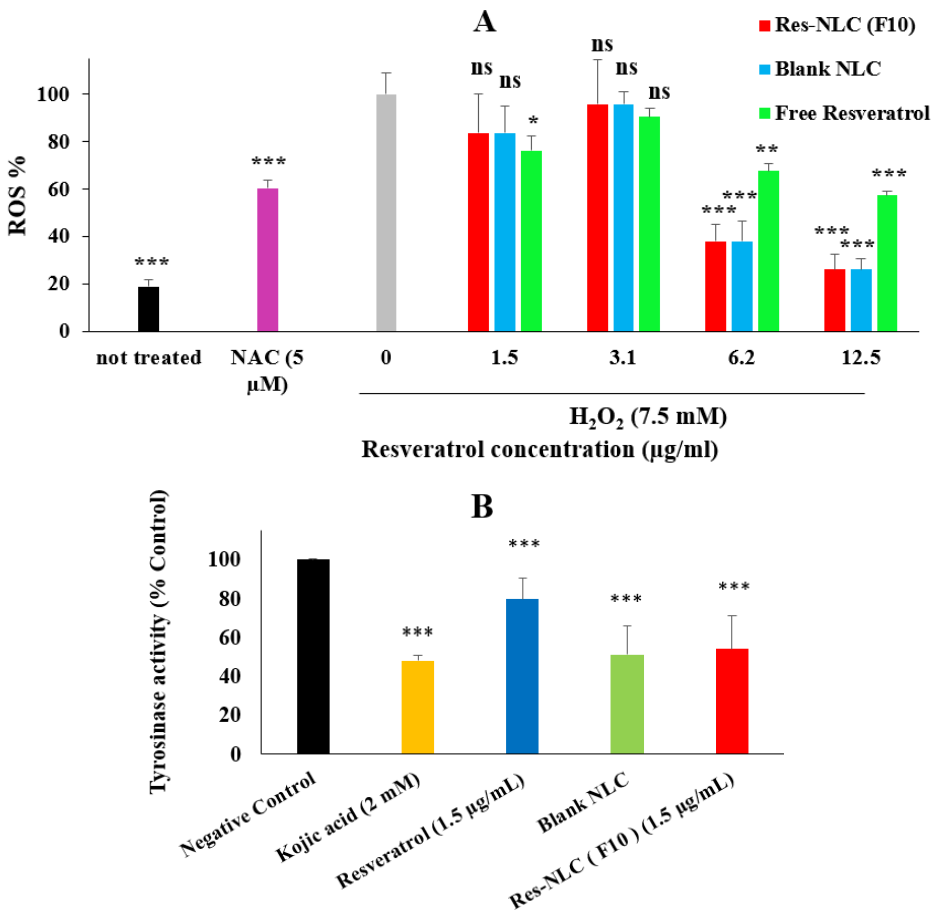

Figure 6. Evaluation of resveratrol in resveratrol-loaded nanostructured lipid carrier (Res-NLC, formulation F10) efficacy on reactive oxygen species (ROS) modulation and tyrosinase activity in B16F10 cells

(A) Intracellular ROS levels in cells pre-exposed for 24 hr to different concentrations of Res-NLC (1.5–12.5 µg/ml), followed by a 2-hour challenge with 7.5 mM H_2O_2. (B) Analysis of tyrosinase activity following 24-hr treatment with free resveratrol (1.5 µg/ml), Res-NLC (1.5 µg/ml), and blank NLC formulations, utilizing kojic acid (2 µM) as a positive control. Data represent the mean±standard deviation (SD) based on three independent biological replicates (n=3). Statistical significance relative to the respective control groups (H_2O_2-treated) is marked with asterisks: *P<0.05, **P<0.01, and ***P<0.001.

protein concentration of 1.1±0.1 mg/ml.

Discussion

Formulation and physicochemical properties and stability of Res-NLCs

The proposed Res-NLC delivery system, utilizing cetyl palmitate as the solid lipid, MCT oil as the liquid lipid, and Tween 80 as the surfactant, is designed to serve as a biocompatible and efficient vehicle for resveratrol. The selection of these components and their respective ratios was based on established pharmacological criteria: A 5% w/w total lipid concentration is frequently utilized in NLC systems to ensure a robust matrix for drug incorporation while maintaining viscosity levels suitable for topical application (39). A solid-to-liquid lipid ratio of 70:30 is effective at preserving the solid lipid matrix, thereby facilitating high drug entrapment efficiency (39). MCT oil is commonly used as a liquid lipid to disrupt the lipid matrix, thereby enhancing both drug-loading capacity and physical stability (39, 40). Tween 80 (Polysorbate 80) is a potent surfactant for NLCs, and concentrations of 3%-6% (w/v) are typically sufficient to ensure formulation stability (39, 40). Resveratrol can be successfully incorporated into NLC formulations at concentrations ranging from 0.1 to 1% w/w (39, 41).

Particle size is a critical parameter for nanocarriers, as it can significantly impact skin penetration and deposition. Research has shown that the optimal particle size range for NLC skin penetration is typically between 100-300 nm (40, 42). Minor adjustments in lipid composition can significantly impact particle size and dispersion quality, while surfactants are essential for reducing emulsion particle size, facilitating homogenization, and improving overall stability (43). Our experimental findings indicated that NLCs formulated with compritol (F4), precirol (F6), or cetyl palmitate (F10) as solid lipids, combined with Tween 80 as the sole surfactant, achieved desirable sizes of <300 nm and demonstrated stability for over one month. Conversely, using tripalmitin (F1-2) or GMS (F7-8) as solid lipids resulted in particles exceeding the 300 nm threshold. The integration of Span 80 into formulations containing compritol or precirol significantly increased the particle size; for instance, the size of the F4 formulation rose from 274 nm to 437 nm (F3) upon the addition of Span 80. Conversely, including Span 80 in formulations with TRP, GMS, or cetyl palmitate reduced particle size. Among the formulations F4, F6, and F10 (all <300 nm), the F10 formulation incorporating cetyl palmitate and Tween 80 demonstrated superior stability over a 1-month observation period, underscoring the need to optimize lipid-surfactant synergy.

The polydispersity index (PDI) is a metric of particle-size uniformity; values<0.5 indicate a narrow distribution, whereas higher values indicate heterogeneity (44). All prepared formulations (F1–F10) exhibited favorable PDI values (<0.35), signifying a uniform particle size distribution. Specifically, formulations F1 and F6 (containing tripalmitin/precirol with 1% Span 80 and 4% Tween 80) displayed PDI values<0.17, while formulations F2 and F10 (containing tripalmitin/cetyl palmitate with 5% Tween 80) achieved the lowest PDI (<0.15), confirming the efficacy of the selected components in producing stable, monodisperse nanoparticles (44, 45).

Zeta potential is a vital indicator of electrostatic repulsion, which helps predict colloidal stability (46). Hydrophilic surfactants enhance NLC stability by promoting surface-layer hydration, thereby preserving nanosuspension integrity through electrostatic and steric interactions (46). While a zeta potential of ±20 mV is generally regarded as indicative of sufficient stability (47), formulations F1-F8 (utilizing 5% Tween 80 or a combination of 4% Tween 80 & 1% Span 80) consistently yielded values below -20 mV. Notably, formulations F9 and F10, formulated with cetyl palmitate, exhibited zeta potential values exceeding -20 mV (Table 2); however, F10 ultimately demonstrated superior overall stability due to combined steric stabilization and matrix properties, indicating that the specific lipid and surfactant network significantly enhances the stability of these systems beyond electrostatic charge alone (45, 48).

TEM confirmed that the particles possessed a spherical morphology, displayed favorable dispersibility, and remained within the nanoscale range. The average diameter of the Res-NLC was determined to be below 200 nm. The observed discrepancy in particle-size measurements between dynamic light scattering (DLS) and TEM is likely due to the differing operating principles of these techniques, compounded by the inherent polydispersity of the samples (24).

DSC was employed to assess the crystallization kinetics of the formulations. The disappearance of the characteristic resveratrol melting peak at 263 °C confirms that the drug was successfully incorporated and solubilized in the lipid phase. Furthermore, the NLC exhibited a lower melting point than its bulk lipid counterpart: Cetyl palmitate had a melting point of 47.3 °C in the NLC formulation, down from 50.3 °C in bulk form. This depression in the melting point is attributed to the inclusion of foreign molecules, specifically the active drug and liquid lipids, within the lipid matrix (48). Additionally, the reduction in enthalpy observed in the blank NLC compared to the pure solid lipid points to a state of heightened crystal disorder and decreased crystallinity within the carrier system (24, 49).

The FT-IR spectra of the Res-NLC formulations were compared against those of pure resveratrol and the constituent lipids. The absence of new spectral peaks indicates that resveratrol was effectively encapsulated within the lipid matrix without undergoing chemical modification or forming new covalent bonds (48).

Encapsulation efficiency (EE%) was determined using the indirect method, yielding results consistent with those from the direct method. Formulation F10 demonstrated a high EE%. Stability testing over a six-month duration showed only a marginal decline in EE%, confirming that resveratrol maintains its chemical integrity when stored within this system (50).

The *in vitro* release studies revealed a sustained, gradual release of resveratrol from the Res-NLC formulation over 48 hr, indicating successful entrapment of the drug within the solid lipid matrix. This release pattern was analogous to that of the Res-emulsion, with drug liberation likely governed by a combination of matrix erosion and diffusion through the lipid network (51). The similarity in the release kinetics between the NLC and emulsion suggests that matrix composition and drug-lipid interactions are more influential determinants of release behavior than particle dimensions alone (51, 52). Ultimately, the release profile is governed by the carrier's structural characteristics, including viscosity and the stabilizing influence of surfactants (52).

Molecular behavior and clustering dynamics of Res-NLCs

The MD simulations highlight clear differences in the organizational behavior of the nanostructured lipid carriers. In the 10 x 10 x 10 nm simulation box, the F10 formulation exhibited a more stable structure, forming one small and one large cluster. This suggests that the interactions within the F10 system are conducive to cluster formation, leading to a more organized structure. Conversely, the F2 system displayed a more fragmented clustering pattern, forming two medium clusters and two small clusters at the edges of the simulation box. This fragmentation indicates reduced stability in the F2 system relative to F10, which is critical for applications requiring stable molecular configurations (53, 54). The R_g is a crucial metric for assessing the compactness of molecular structures. Throughout the simulation period, R_g values for both systems remained nearly constant, indicating stability in their overall dimensions. This similarity in R_g suggests that, despite their differing clustering behaviors, both systems exhibit comparable structural characteristics during the simulation (54). The RMSD analysis provides insight into the structural fluctuations over time. The slight difference in RMSD values between F2 and F10 suggests that the F10 system exhibits greater structural integrity compared to F2. This observation is consistent with the clustering behavior noted earlier, in which F10 exhibited more stable and organized cluster formation (55). A clear quantitative correlation exists between the molecular dynamics simulations and the experimental characteristics of the NLCs. Formulation F10 achieved an optimal particle size within the desirable 100–300 nm dermal range and exhibited exceptional long-term stability, as reflected in the MD simulations by stable, compact clustering behavior. Conversely, formulation F2 yielded an initial particle size greater than 500 nm, which falls outside the acceptable nanocarrier range, and was consequently omitted from long-term stability evaluations. The MD simulations provide a solid molecular explanation for this, as the F2 system exhibited fragmented, less stable clustering, with multiple smaller clusters along the boundaries of the simulation box. This structural inferiority in F2 highlights how unfavorable lipid-surfactant interactions prevent proper matrix compaction during preparation, directly manifesting as larger macroscopic particle sizes and physical instability.

Evaluation of anti-oxidant and anti-tyrosinase potential of Res-NLC

The F10 formulation demonstrated excellent biocompatibility, as evidenced by the lack of significant cytotoxicity observed in B16F10 cells at a 0.5% (V/V) concentration (equivalent to 12.5 µg/ml) following a 24-hour incubation. Oxidative stress, arising from a disruption

of the balance between ROS and anti-oxidant defense mechanisms, can be alleviated by resveratrol by reducing intracellular ROS (56). Experimental results illustrated in Figure 6A confirm that free resveratrol, blank NLC, and Res-NLC effectively mitigate oxidative stress in a dose-dependent manner when compared to the H_2O_2 control group. Notably, the Res-NLC formulation provided superior anti-oxidant and protective effects against free resveratrol, a finding supported by literature indicating that NLCs enhance the stability and bioavailability of compounds otherwise limited by poor solubility (57). By facilitating improved cellular uptake, NLC encapsulation enhances the inherent anti-oxidant properties of resveratrol, yielding greater protection against ROS-induced cellular damage than free resveratrol (58). In addition, the blank NLC formulation demonstrated a notable capacity to modulate intracellular ROS levels. This observation is consistent with prior findings that empty lipid nanocarriers can directly interact with cell membranes and influence cellular oxidative parameters. While encapsulated resveratrol exerts the primary anti-oxidant effect, the carrier's constituent lipids and surfactants also contribute to the overall biological response, underscoring the significance of carrier-cell interactions in topical applications (59). Furthermore, research indicates that resveratrol inhibits melanogenesis by downregulating key proteins, including tyrosinase, TRP-1, and MITF, particularly in UVB-induced pigmentation models. Although free resveratrol exhibits some inhibitory activity, its derivatives demonstrate greater efficacy in skincare applications due to improved stability and bioavailability (60). In this study, the DOPA assay revealed that the Res-NLC F10 formulation significantly outperformed free resveratrol in inhibiting tyrosinase, underscoring its utility as a potential skin-lightening agent, though this requires future confirmation. In summary, these findings highlight Res-NLC systems as promising for skin health and for reducing oxidative stress, though further *in vitro* and *in vivo* evaluations are necessary to refine these formulations for clinical applications.

Despite the promising *in vitro* properties of the F10 formulation, this study has several limitations that should be explicitly acknowledged. These include the lack of ex vivo and *in vivo* topical evaluations, skin permeation and retention data, and formal skin irritation or safety assessments. Furthermore, the biological endpoints were limited to ROS scavenging and tyrosinase inhibition, without incorporating a direct cellular melanin content assay. Additionally, the observed intrinsic activity of blank NLCs, the limited representation in the MD model, and the notable particle growth and physical instability at 37 °C highlight areas that require further optimization. Future investigations will focus on addressing these parameters to ensure clinical translatability.

Conclusion

In this study, a range of novel Res-NLC formulations (F1-10) were developed and systematically evaluated to determine the influence of varying lipid compositions and surfactant mixtures on the nanoparticles' characteristics. The results demonstrate that these formulation parameters significantly affect particle size and surface charge, while maintaining a uniform particle-size distribution across all preparations. Among the tested formulations, F10 emerged as the optimal candidate, exhibiting superior physicochemical characteristics, high entrapment efficiency, and acceptable long-term stability, particularly at 4 °C and 25 °C. At the same time, thermal-dependent particle growth was observed at 37 °C. The *in vitro* release profile of the Res-NLC was comparable to that of Res-emulsion. MD simulations provided further insight, revealing that the F10 system exhibits a more favorable, stable, and organized structural configuration than the F2 system. Biological assays confirmed that the Res-NLC (F10) effectively mitigates oxidative stress by significantly reducing intracellular ROS levels in B10F10 melanoma cells in a concentration-dependent manner. Furthermore, the formulation demonstrated superior efficacy in inhibiting tyrosinase activity compared to free resveratrol, highlighting its anti-oxidant and anti-tyrosinase potential, though further topical validation is warranted. anti-aging and potential skin-lightening agent requiring further validation. While these results underscore the promise of F10 as an effective nanocarrier for topical applications, further research addressing its limitations, including the lack of *ex vivo*/*in vivo* and safety evaluations, skin permeation/retention data, direct melanin assays, blank NLC activity, and thermal instability at 37 °C, is recommended to establish its clinical potential fully.

Acknowledgment

Mashhad University of Medical Sciences supported the research [grant number 4010925].

Authors' Contributions

H AM, Z TN, and S G conceived the study; H AM, M D, and S RH developed the methodology; H AM and M D conducted the investigation and data curation; F H and M N performed the molecular dynamics simulation; V M acquired resources; H AM prepared the original draft; Z TN, V M, and S G reviewed and edited the manuscript; Z TN and S G supervised; Z TN handled project administration. All authors have read and agreed to the published version of the manuscript.

Conflicts of Interest

The authors declare no conflicts of interest.

Declaration

We acknowledge the use of Grammarly to improve the manuscript's English grammar and language style.

References

1. Solomon S, Ivy DJ, Kinnison D, Mills MJ, Neely RR, 3rd, Schmidt A. Emergence of healing in the Antarctic ozone layer. Science 2016; 353:269–274.
2. Wang PW, Hung YC, Lin TY, Fang JY, Yang PM, Chen MH, *et al.* Comparison of the biological impact of UVA and UVB upon the skin with functional proteomics and immunohistochemistry. Antioxidants (Basel) 2019; 8:569.
3. Papaccio F, A DA, Caputo S, Bellei B. Focus on the contribution of oxidative stress in skin aging. Antioxidants (Basel) 2022; 11:1121.
4. Widowati W, Onggowidjaja P, Vosough M, Triharsiwin DN, Distya AP, Nurani LW, *et al.* Hepatoprotective effect of hUC-MSC secretome in LPS-induced HepG2 cells. Iran J Basic Med Sci 2026; 29: 901-908.
5. Rostahi H, Aramshahi SMA, Vosoughi N, Shamlou S, Shahmahmoudi Z, Milan P, *et al.* Enhanced effects of Wharton's jelly-derived MSC secretome and microbial exopolysaccharide on

cellular responses and tissue repair in diabetic wound healing. Iran J Basic Med Sci 2026; 29: 1747-1758.
6. Nasiri N, Hemmati P, Tabaie SM. Conditioned medium from mesenchymal stem cells: Towards skin tissue engineering and wound healing. Iran J Basic Med Sci 2026; 29: 181-190.
7. Dall'Olmo L, Papa N, Surdo NC, Marigo I, Mocellin S. Alpha-melanocyte stimulating hormone (α-MSH): Biology, clinical relevance and implication in melanoma. J Transl Med 2023; 21:562.
8. Netcharoensirisuk P, Umehara K, De-Eknamkul W, Chaotham C. Cajanin suppresses melanin synthesis through modulating MITF in human melanin-producing cells. Molecules 2021; 26:6040.
9. Solano F. Photoprotection and skin pigmentation: Melanin-related molecules and some other new agents obtained from natural sources. Molecules 2020; 25:1537.
10. Fernandes MS, Kerkar S. Microorganisms as a source of tyrosinase inhibitors: A review. Annals of Microbiol 2017; 67:343–358.
11. Panzella L, Napolitano A. Natural and bioinspired phenolic compounds as tyrosinase inhibitors for the treatment of skin hyperpigmentation: Recent advances. Cosmetics 2019; 6:57.
12. Song H, Hwang YJ, Ha JW, Boo YC. Screening of an epigenetic drug library identifies 4-((hydroxyamino) carbonyl)-N-(2-hydroxyethyl)-N-phenyl-benzeneacetamide that reduces melanin synthesis by inhibiting tyrosinase activity independently of epigenetic mechanisms. Int J Mol Sci 2020; 21:4589.
13. Saewan N, Jimtaisong A. Photoprotection of natural flavonoids. J Appl Pharm Sci 2013; 3:129–141.
14. Jatana S, Palmer BC, Phelan SJ, Gelein R, DeLouise LA. *In vivo* quantification of quantum dot systemic transport in C57BL/6 hairless mice following skin application post-ultraviolet radiation. Part Fibre Toxicol 2017; 14:12.
15. Sharma B, Iqbal B, Kumar S, Ali J, Baboota S. Resveratrol-loaded nanoemulsion gel system to ameliorate UV-induced oxidative skin damage: From *in vitro* to *in vivo* investigation of anti-oxidant activity enhancement. Arch Dermatol Res 2019; 311:773–793.
16. Ungvari Z, Bagi Z, Feher A, Recchia FA, Sonntag WE, Pearson K, *et al.* Resveratrol confers endothelial protection via activation of the anti-oxidant transcription factor Nrf2. Am J Physiol Heart Circ Physiol 2010; 299:H18–H24.
17. Alavi M, Farkhondeh T, Aschner M, Samarghandian S. Resveratrol mediates its anti-cancer effects by Nrf2 signaling pathway activation. Cancer Cell International 2021; 21:1–9.
18. Marko M, Pawliczak R. Resveratrol and its derivatives in inflammatory skin disorders—atopic dermatitis and psoriasis: A review. Antioxidants (Basel) 2023; 12:1954.
19. Mascarenhas-Melo F, Araújo ARTS, Rodrigues M, Mathur A, Gonçalves MBS, Tanwar K, *et al.* Dermatological bioactivities of resveratrol and nanotechnology strategies to boost its efficacy—An updated review. Cosmetics 2023; 10:68.
20. Hecker A, Schellnegger M, Hofmann E, Luze H, Nischwitz SP, Kamolz LP, *et al.* The impact of resveratrol on skin wound healing, scarring, and aging. Int Wound J 2022; 19:9–28.
21. Gokce EH, Korkmaz E, Dellera E, Sandri G, Bonferoni MC, Ozer O. Resveratrol-loaded solid lipid nanoparticles versus nanostructured lipid carriers: evaluation of anti-oxidant potential for dermal applications. Int J Nanomedicine 2012; 7:1841–1850.
22. Shimojo AAM, Fernandes ARV, Ferreira NRE, Sanchez-Lopez E, Santana MHA, Souto EB. Evaluation of the influence of process parameters on the properties of resveratrol-loaded NLC using 22 full factorial design. Antioxidants 2019; 8:272.
23. Freire TB, Pinto CASdO, Gonçalves MIdA, Serra CHdR, Dario MF, Baby AR, *et al.* Impact of ferulic acid and resveratrol on the effectiveness and safety of sunscreen. Braz J Pharm Sci 2023; 59:e23357.
24. Atapour-Mashhad H, Nejabat M, Hadizadeh F, Hoseinsalari A, Golmohammadzadeh S. Preparation, characterization, and molecular dynamic simulation of novel coenzyme Q10 loaded nanostructured lipid carriers. Curr Pharm Des 2023; 29:2177–2190.
25. Vaziri MS, Tayarani-Najaran Z, Kabiri H, Nasirizadeh S, Golmohammadzadeh S, Kamali H. Preparation and characterization of Undecylenoyl Phenylalanine loaded-nanostructure lipid carriers (NLCs) as a new α-MSH Antagonist and antityrosinase agent. Adv Pharm Bull 2022; 13:290.
26. Moradi A, Seifati SM, Darroudi M, Golmohammadzadeh S, Ashkezari MD. Nanocrystal structure of minoxidil: A safe stimulator for hair growth factor for C57BL/6 mice. Curr Med Chem 2025; 32:4343–4355.
27. Kabiri H, Tayarani-Najaran Z, Rahmanian-devin P, Vaziri MS, Nasirizadeh S, Golmohammadzadeh S, *et al.* Preparation, characterization, and evaluation of anti-tyrosinase activity of solid lipid nanoparticles containing Undecylenoyl phenylalanine (Sepiwhite®). J Cosmet Dermatol 2022; 21:6061–6071.
28. Smith BC. Fundamentals of Fourier Transform Infrared Spectroscopy: CRC press; 2011.
29. He Y, Li H, Zheng X, Yuan M, Yang R, Yuan M, *et al.* Preparation, *in vivo* and *in vitro* release of polyethylene glycol monomethyl ether-polymandelic acid microspheres loaded panax notoginseng saponins. Molecules 2019; 24:2024.
30. Van Der Spoel D, Lindahl E, Hess B, Groenhof G, Mark AE, Berendsen HJC. GROMACS: fast, flexible, and free. J Comput Chem 2005; 26:1701–1718.
31. Hess B, Bekker H, Berendsen HJC, Fraaije JGEM. LINCS: A linear constraint solver for molecular simulations. J Comput Chem 1997; 18:1463–1472.
32. Bussi G, Donadio D, Parrinello M. Canonical sampling through velocity rescaling. J Chem Phys 2007; 126:014101.
33. Berendsen HJC, Postma JPMv, Van Gunsteren WF, DiNola A, Haak JR. Molecular dynamics with coupling to an external bath. J Chem Phys 1984; 81:3684–3690.
34. Atapour-Mashhad H, Soukhtanloo M, Golmohammadzadeh S, Chamani J, Nejabat M, Hadizadeh F. Synthesis and molecular dynamic simulation of novel cationic and non-cationic pyrimidine derivatives as potential G-quadruplex-ligands. Anticancer Agents Med Chem 2024; 24:1126–1141.
35. Hoseinsalari A, Atapour-Mashhad H, Asili J, Tayarani-Najaran Z, Mohtashami L, Khanavi M, *et al.* Preparation and characterization of nanostructured lipid carriers (NLCs) containing glycyrrhiza glabra extract for the treatment of skin hyperpigmentation. Curr Pharm Des 2024; 30:3213–3232.
36. Im YS, Ryu YK, Moon EY. Mouse melanoma cell migration is dependent on production of reactive oxygen species under normoxia condition. Biomol Ther (Seoul) 2012; 20:165–170.
37. Hashemi-Shahri SH, Golshan A, Mohajeri SA, Baharara J, Amini E, Salek F, *et al.* ROS-scavenging and Anti-tyrosinase Properties of Crocetin on B16F10 Murine Melanoma Cells. Anticancer Agents Med Chem 2018; 18:1064–1069.
38. Ghasemiyeh P, Azadi A, Daneshamouz S, Heidari R, Azarpira N, Mohammadi-Samani S. Cyproterone acetate-loaded nanostructured lipid carriers: Effect of particle size on skin penetration and follicular targeting. Pharm Dev Technol 2019; 24:812–823.
39. Elmowafy M, Al-Sanea MM. Nanostructured lipid carriers (NLCs) as drug delivery platform: Advances in formulation and delivery strategies. Saudi Pharm J 2021; 29:999–1012.
40. Kim MH, Kim KT, Sohn SY, Lee JY, Lee CH, Yang H, *et al.* Formulation and evaluation of nanostructured lipid carriers (NLCs) Of 20(S)-protopanaxadiol (PPD) by box-behnken design. Int J Nanomedicine 2019; 14:8509–8520.
41. Masoomzadeh S, Sadighian S, Gholikhani T, Rostamizadeh K. Potential use of nanostructured lipid carriers mediated neuronal delivery of carbamazepine. Nanomed Res J 2022; 7:330–337.
42. Mardhiah Adib Z, Ghanbarzadeh S, Kouhsoltani M, Yari Khosroshahi A, Hamishehkar H. The effect of particle size on the deposition of solid lipid nanoparticles in different skin layers: A histological study. Adv Pharm Bull 2016; 6:31–36.
43. Corrigan DO, Healy AM, Corrigan OI. Preparation and release of salbutamol from chitosan and chitosan co-spray dried compacts and multiparticulates. Eur J Pharm Biopharm 2006; 62:295–305.
44. Danaei M, Dehghankhold M, Ataei S, Hasanzadeh Davarani

F, Javanmard R, Dokhani A, *et al.* Impact of particle size and polydispersity index on the clinical applications of lipidic nanocarrier systems. Pharmaceutics 2018; 10:57.
45. Pizzol CD, Filippin-Monteiro FB, Restrepo JA, Pittella F, Silva AH, Alves de Souza P, *et al.* Influence of surfactant and lipid type on the physicochemical properties and biocompatibility of solid lipid nanoparticles. Int J Environ Res Public Health 2014; 11:8581–8596.
46. Pochapski DJ, Carvalho dos Santos C, Leite GW, Pulcinelli SH, Santilli CV. Zeta potential and colloidal stability predictions for inorganic nanoparticle dispersions: Effects of experimental conditions and electrokinetic models on the interpretation of results. Langmuir 2021; 37:13379–13389.
47. Tamjidi F, Shahedi M, Varshosaz J, Nasirpour A. Design and characterization of astaxanthin-loaded nanostructured lipid carriers. Innov Food Sci Emerg Technol 2014; 26:366–374.
48. Atapour-Mashhad H, Tayarani-Najaran Z, Golmohammadzadeh S. Preparation and characterization of novel nanostructured lipid carriers (NLC) and solid lipid nanoparticles (SLN) containing coenzyme Q10 as potent anti-oxidants and antityrosinase agents. Heliyon 2024; 10:e31429.
49. Gomes MJ, Martins S, Ferreira D, Segundo MA, Reis S. Lipid nanoparticles for topical and transdermal application for alopecia treatment: Development, physicochemical characterization, and *in vitro* release and penetration studies. Int J Nanomedicine 2014; 9:1231–1242.
50. Jayan H, Leena MM, Sundari SKS, Moses JA, Anandharamakrishnan C. Improvement of bioavailability for resveratrol through encapsulation in zein using electrospraying technique. J Funct Foods 2019; 57:417–424.
51. Balata GF, Essa EA, Shamardl HA, Zaidan SH, Abourehab MA. Self-emulsifying drug delivery systems as a tool to improve solubility and bioavailability of resveratrol. Drug Des Devel Ther 2016; 10:117–128.
52. Tang H, Xiang S, Li X, Zhou J, Kuang C. Preparation and *in vitro* performance evaluation of resveratrol for oral self-microemulsion. PLoS One 2019; 14:e0214544.
53. Yu M, Shen Z, Zhang S, Zhang Y, Zhao H, Zhang L. The active components of Erzhi wan and their anti-Alzheimer's disease mechanisms determined by an integrative approach of network pharmacology, bioinformatics, molecular docking, and molecular dynamics simulation. Heliyon 2024; 10:e33761.
54. Chen H, Levitas VI, Popov D, Velisavljevic N. Nontrivial nanostructure, stress relaxation mechanisms, and crystallography for pressure-induced Si-I→ Si-II phase transformation. Nature Communications 2022; 13:982.
55. Yin LL, Xu JK, Wang XJ, Gao SQ, Lin YW. Molecular dynamics simulation and kinetic study of fluoride binding to V21C/V66C myoglobin with a cytoglobin-like disulfide bond. Int J Mol Sci 2020; 21:2512.
56. Jomova K, Raptova R, Alomar SY, Alwasel SH, Nepovimova E, Kuca K, *et al.* Reactive oxygen species, toxicity, oxidative stress, and anti-oxidants: chronic diseases and aging. Arch Toxicol 2023; 97:2499–2574.
57. Astley C, Houacine C, Zaabalawi A, Wilkinson F, Lightfoot AP, Alexander Y, *et al.* Nanostructured lipid carriers deliver resveratrol, restoring attenuated dilation in small coronary arteries, via the AMPK pathway. Biomedicines 2021; 9:1852.
58. Radeva L, Stefanova D, Yordanov Y, Kamenova K, Petrov PD, Marinova MK, *et al.* Incorporation of resveratrol in polymeric nanogel for improvement of its protective effects on cellular and microsomal oxidative stress Models Gels 2023; 9:450.
59. Brugè F, Damiani E, Puglia C, Offerta A, Armeni T, Littarru GP, *et al.* Nanostructured lipid carriers loaded with CoQ10: Effect on human dermal fibroblasts under normal and UVA-mediated oxidative conditions. Int J Pharm 2013; 455:348–356.
60. Lee TH, Seo JO, Baek SH, Kim SY. Inhibitory effects of resveratrol on melanin synthesis in ultraviolet B-induced pigmentation in Guinea pig skin. Biomol Ther (Seoul) 2014; 22:35–40.